

# Comparison of Nonlinear Force-free Field and Potential Field in the Quiet Sun

*Solar Physics*

S. Liu<sup>1</sup> · H.Q. Zhang<sup>1</sup> · J.T. Su<sup>1</sup>

© Springer ●●●

**Abstract** In this paper, a potential field extrapolation and three nonlinear force-free (NLFF) field extrapolations (optimization, direct boundary integral (DBIE) and approximate vertical integration (AVI) methods) are used to study the spatial configuration of magnetic field in the quiet Sun. It is found that the strength differences between the three NLFF and potential fields exist in the low layers. However, they tend to disappear as the height increases, which are of the order of 0.1 G when the height exceeds  $\sim 2000$  km above the photosphere. The absolute azimuth difference between one NLFF field and the potential field is as follows: for the optimization field, it decreases evidently as the height increases; for the DBIE field, it almost keeps constant and shows no significant change as the height increases; for the AVI field, it increases slowly as the height increases. The analysis shows that the reconstructed NLFF fields deviate significantly from the potential field in the quiet Sun.

**Keywords:** Quiet Sun, Magnetic field, Chromosphere

## 1. Introduction

Although a large amount of studies focused on the magnetic field of solar active regions, it is very important to know the spatial configuration of magnetic field in the quiet Sun since most part of solar surface are covered by the quiet regions even in the solar maximum years. Due to the restrictions of observational technique, the accurate information about how the magnetic field transport in the solar chromosphere and corona is still not clear. Theoretically, Gabriel (1976) predicted that the magnetic field expands from the photosphere into the chromosphere and corona to form a canopy-like structure. At present, it is still difficult to check Gabriel's suggestion from the observations. In spite of that, the relations between the photospheric magnetic field and the chromospheric and coronal features may provide some important but limited information about the expansion of magnetic field.

---

Key Laboratory of Solar Activity, National Astronomical Observatory, Chinese Academy of Sciences, Beijing, China  
email: lius@nao.cas.cn

Some authors studied the relations between the photospheric and chromospheric magnetic field (*i.g.*, Zhang, 1996; Almeida, 1997; Démoulin *et al.*, 1997; Cuperman, Bruma and Heristchi, 1997; Zhang and Zhang, 1999; Zhang and Zhang, 2000a; Zhang and Zhang, 2000b and Harvey, 2006a). For example, Zhang (1996) argued that the magnetic field of the active regions extends up into the chromosphere in the fibril forming from the photosphere. Zhang and Zhang (2000a) found there are similarities between the chromospheric and photospheric magnetograms in the quiet Sun. Some other authors studied the relations between the magnetic fields in the photosphere and transition regions/corona (*i.g.*, Giovanelli 1980; Dowdy *et al.* 1986; Schrijver *et al.* 2003; Harvey 2006b; Philip 2008 and Dimitropoulou *et al.* 2009). For example, Schrijver *et al.* (2003) argued that relatively strong internetwork field lines close back within several thousand kilometers. Dimitropoulou *et al.* (2009) found that there are no direction correlations between the fractal dimensions of the 2D photospheric patterns and their 3D counterparts in the corona at the nonlinear force-free limit, but there are significant correlations between the fractal dimensions of the photospheric and coronal structures for the potential and linear force-free (LFF) extrapolation.

The magnetic field extrapolation with force-free assumption (Aly, 1989) is an alternative method to study the configuration of the solar magnetic field based on the observations of photospheric magnetic field. The merit is that it can give the adequate spatial information of the solar magnetic field. Generally, most of the extrapolated fields have been used to describe the topology of magnetic field in the active regions (*e.g.*, Régnier *et al.*, 2002; Régnier and Amari, 2004; Wiegmann *et al.*, 2006; Song *et al.*, 2006; Song *et al.*, 2007; He, Wang and Yan, 2008; Schrijver *et al.*, 2008; Jing, 2008 and DeRosa *et al.*, 2009). However, as measurements of the vector magnetic fields of active regions are more reliable than those of the quiet Sun (*e.g.*, better signal-to-noise ratio in strong field areas). Moreover, force-free assumption is even more widely violated in the quiet Sun than in the active regions, therefore so far very few studies applied extrapolation techniques to study the configuration of magnetic field in the quiet Sun. Régnier *et al.* (2008) used the magnetic field extrapolation to derive the null points density in the quiet Sun. Tu *et al.* (2005) used the magnetic field extrapolation to study the origin of solar wind and give the 3D structure of magnetic field in a quiet Sun. They found that there is no canopy shape as originally suggested, but the cross section of magnetic flux increases almost linearly with height. Their study is consistent with the results by Zhang and Zhang (2000b). However, the method used in above studies is the potential field approximation or LFF field extrapolation. Since the magnetic field in the quiet Sun is non-potential (Woodard and Chae, 1999; Zhao *et al.*, 2009), use of the NLFF field extrapolation is more reasonable than that of the linear force-free extrapolation. Therefore, the difference between the NLFF field and the potential field in the quiet Sun is an important subject to study.

At present, the potential and LFF field extrapolations reached a mature development. In this case, only the line-of-sight (LOS) component of the magnetic field is taken as the boundary condition (*e.g.*, Chiu and Hilton, 1977; Seehafer, 1978; Alissandrakis, 1981; Gary, 1989). For the NLFF field extrapolation, which, on the contrary, requires the knowledge of the vector field at the

photosphere, recently several models and methods have been proposed (*e.g.*, Wu *et al.*, 1990; Amari *et al.*, 1997; Sakurai, 1981; Chodura and Schlueter, 1981; Yan and Sakurai, 2000; Wheatland *et al.*, 2000; Wiegelmann, 2004; Song *et al.*, 2006; He and Wang, 2008). Most of these methods can give reliable results that satisfy force-free assumption (*e.g.*, Schrijver *et al.*, 2006; Amari *et al.*, 2006; Song *et al.*, 2006; Valori *et al.*, 2007). In applications to the measured magnetograms from the active regions, the reliability of the extrapolated fields is often assessed by checking the morphological consistence between the NLFF model field lines and the observed features such as coronal loops observed in EUV and X-ray images (*e.g.*, Régnier and Amari, 2004; Wiegelmann *et al.*, 2006 and Régnier *et al.*, 2007). However, at present there is no such work that uses the NLFF field extrapolation to study the configuration of magnetic field in the quiet Sun, mainly because the vector magnetograms in the quiet Sun before the *Hinode* were not very suitable for the application of NLFF extrapolation. Fortunately, Spectro-Polarimeter (SP) of the Solar Optical Telescope (SOT) on board *Hinode* (Kosugi *et al.*, 2007; Tsuneta *et al.*, 2008; Ichimoto *et al.*, 2008) has been used to measure the vector magnetic field in the quiet Sun with very high spatial resolution and adequate sensitivity for the first time. This gives us a chance to extrapolate the NLFF magnetic field in the quiet Sun.

Organization of this paper is as follows: firstly, the description of employed data and the extrapolation methods will be introduced in Section 2, secondly, the comparisons between the NLFF fields and the potential field are shown in Section 3, at last, the discussions and conclusions will be given in section 4.

## 2. Data processing and extrapolation methods

### 2.1. Data processing

A quiet region observed by *Hinode* SOT/SP on April 16, 2007 from 00:23 UT to 01:48 UT is used in this work. The SP obtains line profiles of two magnetically sensitive Fe lines at 630.15 and 630.25 nm and nearby continuum. Spectra are exposed and read out continuously 16 times per rotation of the polarization modulator, and the raw spectra are added and subtracted onboard in real time to demodulate, generating Stokes *IQUV* spectral images. The parameters relevant to the vector magnetic field, which are derived from the inversion of the full Stokes profiles based on the assumption of the Milne-Eddington (ME) atmospheric model, are the total field strength  $B$ , the inclination angle  $\gamma$  with respect to the (LOS) direction, the azimuth angle  $\phi$  and the filling factor  $f$ . Following Lites *et al.* (1999) and Zhao *et al.* (2009), the longitudinal component of the spatially resolved vector field is obtained with the expression  $fB\cos(\gamma)$ , and the transverse component  $\sqrt{f}B\sin(\gamma)$ . We use the acute angle method (Wang *et al.*, 1994; Wang, 1997; Wang *et al.*, 2001 and Metcalf *et al.*, 2006) to resolve 180° ambiguity, in which the observed field is compared to the extrapolated potential field at the photosphere. The orientation of the observed transverse component is chosen by requiring that  $-90^\circ \leq \Delta\theta \leq 90^\circ$ , where  $\Delta\theta = \theta_o - \theta_e$  is the angle between the observed and extrapolated transverse components.

Figure 1A shows the LOS magnetogram of this quiet region observed by *Hinode* SOT/SP. Figure 1B is the vector magnetogram that is employed as the extrapolation boundary in this work, and it corresponds to the region that is highlighted by a white square in Figure 1A. The size of the employed vector magnetogram is  $100 \times 100$  pixels with a resolution of  $0.148''$  in x-direction and  $0.159''$  in y-direction. It is located near the solar disk center ( $-5.2''$  and  $7.3''$  in X-Y direction of the heliographic coordinates). In our work the altitude of extrapolated fields is limited in 50 pixels and its resolution is  $0.148''$  in z-direction.

## 2.2. Four extrapolation methods

The force-free assumption requires the magnetic field to satisfy the following equations,

$$\nabla \times \mathbf{B} = \alpha(\mathbf{r})\mathbf{B}, \quad (1)$$

$$\nabla \cdot \mathbf{B} = 0, \quad (2)$$

They imply that there is no Lorentz force and  $\alpha$  is constant along magnetic field lines. If  $\alpha = 0$ , the equations represent a potential field (a current-free field). If  $\alpha = \text{constant}$ , they describe a current-carrying LFF field; if  $\alpha = f(\mathbf{r})$  they describe a general NLFF field.

In this paper, the LFF extrapolation method (Seehafer, 1978) is used to calculate the potential field by choosing  $\alpha = 0$ . This method gives the components of the magnetic field in terms of a Fourier series. The photospheric magnetogram that covers a region with a length of  $L_x$  in x-direction and a length of  $L_y$  in y-direction is artificially extended to a rectangular region covering  $-L_x$  to  $L_x$  and  $-L_y$  to  $L_y$  by taking an antisymmetric mirror image of the original magnetogram. For example,  $B_z(-x, y) = -B_z(x, y)$  and  $B_z(x, -y) = -B_z(x, y)$ . The expression for the magnetic field is given by

$$B_x = \sum_{m,n=1}^{\infty} \frac{C_{mn}}{\lambda_{mn}} \exp(-r_{mn}z) \left[ \alpha \frac{n\pi}{L_y} \sin\left(\frac{m\pi x}{L_x}\right) \cos\left(\frac{n\pi y}{L_y}\right) - r_{mn} \frac{m\pi}{L_x} \cos\left(\frac{m\pi x}{L_x}\right) \sin\left(\frac{n\pi y}{L_y}\right) \right], \quad (3)$$

$$B_y = - \sum_{m,n=1}^{\infty} \frac{C_{mn}}{\lambda_{mn}} \exp(-r_{mn}z) \left[ \alpha \frac{m\pi}{L_x} \cos\left(\frac{m\pi x}{L_x}\right) \sin\left(\frac{n\pi y}{L_y}\right) + r_{mn} \frac{n\pi}{L_y} \sin\left(\frac{m\pi x}{L_x}\right) \cos\left(\frac{n\pi y}{L_y}\right) \right], \quad (4)$$

$$B_z = \sum_{m,n=1}^{\infty} C_{mn} \exp(-r_{mn}z) \sin\left(\frac{m\pi x}{L_x}\right) \sin\left(\frac{n\pi y}{L_y}\right), \quad (5)$$

with  $\lambda_{mn} = \pi^2(m^2/L_x^2 + n^2/L_y^2)$  and  $r_{mn} = \sqrt{\lambda_{mn} - \alpha^2}$ . The coefficients  $C_{mn}$  are obtained by taking the FFT of  $B_z$  at  $z = 0$ .

The optimization method presented by Wheatland *et al.* (2000) and developed by Wiegmann (2004) consists in minimizing a joint measure for the normalized Lorentz force and the divergence of the field, given by the function,

$$L = \int_V \omega(x, y, z) [B^{-2} |(\nabla \times \mathbf{B} \times \mathbf{B})|^2 + |\nabla \cdot \mathbf{B}|^2] d^3x, \quad (6)$$

where  $\omega(x, y, z)$  is a weighting function. It is evident that (for  $w > 0$ ) the force-free equations are fulfilled when  $L$  is equal to zero. This method involves minimizing  $L$  by optimizing the solution function  $\mathbf{B}(x, t)$  through states that are increasingly force- and divergence-free, where  $t$  is an artificial time-like parameter. The relevant theories and algorithms can be found in the papers of Wheatland *et al.* (2000) and Wiegmann (2004).

The direct boundary integral equation (DBIE) method (Yan and Li, 2006; He and Wang, 2008) is developed from the BIE method proposed by Yan and Sakurai (2000), which uses the Green function to extrapolate the magnetic field. In this method, an optimized parameter  $\lambda$ , defined in the papers of Yan and Li (2006), must be found through iteration. The integral

$$\mathbf{B}(x_i, y_i, z_i) = \int_{\Gamma} \frac{z_i [\lambda r \sin(\lambda r) + \cos(\lambda r)] \mathbf{B}_0(x, y, 0)}{2\pi [(x - x_i)^2 + (y - y_i)^2 + z_i^2]^{3/2}}, \quad (7)$$

is used to calculate the magnetic field, where  $r = [(x - x_i)^2 + (y - y_i)^2 + z_i^2]^{1/2}$  and  $\mathbf{B}_0$  is the magnetic field of photospheric surface. The detailed theories can be found in the papers of He and Wang (2008) and Yan and Sakurai (2000).

The approximate vertical integration (AVI) method (Song *et al.*, 2006) was improved from the direct integration proposed by Wu *et al.* (1990). In this method, the magnetic field is given by the following formula,

$$\mathbf{B}_x = \xi_1(x, y, z) F_1(x, y, z), \quad (8)$$

$$\mathbf{B}_y = \xi_2(x, y, z) F_2(x, y, z), \quad (9)$$

$$\mathbf{B}_z = \xi_3(x, y, z) F_3(x, y, z), \quad (10)$$

assuming the second-order continuous partial derivatives in a certain height range,  $0 < z < H$  ( $H$  is the calculated height from the photospheric surface). In Equations (8)-(10),  $\xi_1, \xi_2$  and  $\xi_3$  mainly depend on  $z$  and slowly vary with  $x$  and  $y$ , while  $F_1, F_2$  and  $F_3$  mainly depend on  $x$  and  $y$  and weakly vary with  $z$ , which are mathematical representation of the similarity solutions. After constructing the magnetic field, the following integration equations,

$$\frac{\partial B_x}{\partial z} = \frac{\partial B_z}{\partial x} + \alpha B_y, \quad (11)$$

$$\frac{\partial B_y}{\partial z} = \frac{\partial B_z}{\partial y} - \alpha B_x, \quad (12)$$

$$\frac{\partial B_z}{\partial z} = -\frac{\partial B_x}{\partial x} - \frac{\partial B_y}{\partial y}, \quad (13)$$

$$\alpha B_z = \frac{\partial B_y}{\partial x} - \frac{\partial B_x}{\partial y}, \quad (14)$$

are used to carry out the extrapolation. The detailed descriptions are described in the paper of Song *et al.* (2006).

### 3. Results

Conventionally, the quiet Sun is considered far from force-free, thus the force-free extent of the selected area on the photosphere should be investigated. Three parameters  $F_x/F_p$ ,  $F_y/F_p$  and  $F_z/F_p$ , where  $F_x$ ,  $F_y$ ,  $F_z$  and  $F_p$  are defined in the following forms (Metcalf *et al.* 1995 and Moon *et al.* 2002),

$$F_x = -\frac{1}{4\pi} \int B_x B_z dx dy, \quad (15)$$

$$F_y = -\frac{1}{4\pi} \int B_y B_z dx dy, \quad (16)$$

$$F_z = \frac{1}{8\pi} \int (B_z^2 - B_x^2 - B_y^2) dx dy, \quad (17)$$

$$F_p = \frac{1}{8\pi} \int (B_z^2 + B_x^2 + B_y^2) dx dy, \quad (18)$$

are used to check the force-free condition of this quiet region. In Equations (15)-(18),  $F_x$ ,  $F_y$ ,  $F_z$  are the components of the Lorentz force and  $F_p$  is a characteristic magnitude of the total Lorentz force. For this quiet region (Figure 1B),  $F_x/F_p$ ,  $F_y/F_p$  and  $F_z/F_p$  are found to be 0.03, -0.01 and -0.35, respectively. Metcalf *et al.* (1995) argued that the magnetic fields with  $|F_z/F_p| \sim 0.1$  can be called force-free. Moon *et al.* (2002) studied 12 vector magnetograms and obtained  $|F_z/F_p|$  ranging from 0.06 to 0.32 with a median value of 0.13. They concluded that the photospheric magnetic fields are not so far from force-free. Although  $|F_z/F_p|$  of this quiet region is a little larger than those of the active regions studied by Moon *et al.* (2002), we tentatively apply the force-free extrapolation to reconstruct the magnetic fields above the quiet region.

Since the extrapolated fields are approximate solutions of the force-free equations, their degree of force- and divergence-freeness should be checked first. Wheatland *et al.* (2000) introduced the criterion of force-freeness  $\sigma_J$ ,

$$\sigma_J = \frac{\sum_i J_i \sigma_i}{\sum_i J_i}, \quad (19)$$

where

$$\sigma_i = \sin\theta_i = \frac{|\mathbf{J} \times \mathbf{B}|_i}{J_i B_i}, \quad (20)$$

and the criterion of divergence-freeness  $f_i$ ,

$$f_i = \frac{\int_{\Delta S_i} \mathbf{B} \cdot d\mathbf{S}}{\int_{\Delta S_i} |\mathbf{B}| d\mathbf{S}} \approx \frac{(\nabla \cdot \mathbf{B})_i \Delta V_i}{B_i A_i}, \quad (21)$$

to assess the quality of the extrapolations.  $\sigma_J$  indicates the weighted average of the sine of angle between the current density and magnetic field. The average value of the magnitude of  $f_i$  is used to check if the system is close to divergence free, where  $A_i$  is the surface area of the small volume. The values of  $\sigma_J$  and  $\langle |f_i| \rangle$  should be equal to zero, if the force- and divergence-freeness of extrapolated field are fully satisfied.

Table 1 gives the values of  $\sigma_J$  and  $\langle |f_i| \rangle$  in the four extrapolated fields. The maximum value of Lorentz force ( $F_{max} = \max(|\mathbf{J}_i \times \mathbf{B}_i|)$ , where  $\mathbf{J}_i = \nabla \times \mathbf{B}_i$ ) and the ratio of the total magnetic energy of the NLFF extrapolated fields to that of the potential field ( $\varepsilon = E_{NLFF}/E_{pote}$ ) in the total volume are also given in the Table 1. It can be found that these four extrapolated fields meet the force- and divergence-freeness basically and the orders of magnitude of these criteria are the same for all the extrapolated fields. It is also found that the potential field is computed with the highest degree of consistency, because  $\sigma_J$  and  $\langle |f_i| \rangle$  of the potential field are all smaller than those of three NLFF fields. For the NLFF extrapolated fields, the divergence-freeness of the optimization field is the best among these three NLFF fields, because  $\langle |f_i| \rangle$  in the optimization field is smaller than those in the other two NLFF fields. The AVI field is reconstructed with the best force-freeness, which can be seen from the value of  $\sigma_J$  and  $F_{max}$  of these NLFF fields.  $\varepsilon$  is 1.98, 2.10 and 2.81 for optimization, DBIE and AVI extrapolated fields, respectively, which indicate that these NLFF fields are reconstructed with a high degree of non-potentiality since the values of  $\varepsilon$  deviate strongly from unity.

Figure 2 shows the magnetic field lines of these four extrapolated fields, where the red lines are the closed field lines and the blue ones the open field lines (here the term of open is used to characterize the field lines that leaves through the upper or lateral boundary of the extrapolation box). It is found that the topological structures of these extrapolated magnetic field lines are similar on the whole, but the open magnetic field lines of the NLFF fields are more than those of the potential field. To see the distributions of the magnetic field lines clearly and to find their differences, a green square region is cut near the disk center shown in Figure 2, and the magnetic field lines in the region are shown in Figure 3. It can be seen that the open magnetic field lines tend to be located at the strong field region basically. A part of the closed magnetic field lines of the NLFF fields can reach higher altitudes than those of the potential field, and these closed lines are more vertical than the potential one. Note that the extending trends of the open magnetic field lines of the optimization field are similar to those of the potential field. The reason may be that the initial condition of the optimization field is a potential field, but there are no such initial conditions for the AVI and DBIE methods. In figure 3, it can also be seen that on the whole, the distributions of the magnetic field lines of the AVI and DBIE fields are similar, especially for closed magnetic field lines located at the lower heights.

To compare these extrapolated fields, horizontal cuts of the four extrapolated fields at three layers ( $z = 109, 545$  and  $2180$  km) are shown in Figure 4, where their similarities and differences are displayed evidently. On the whole, the LOS components of these extrapolated fields look similar and the expansion amplitudes of these fields are almost the same. On the other hand, the transverse magnetic fields are different, especially for their azimuths. For the AVI and DBIE extrapolated fields, the arrows of the transverse fields run across the strong LOS field regions as the height increases, e.g. region A labeled in the third row. It also can be found that though some fine features are different, the similarities still exist between the transverse magnetic fields extrapolated with the DBIE and AVI methods. For the potential and optimization fields, the arrows of the transverse fields are inclined to converge in the strong negative polarity region and diverge in the strong positive polarity region.

In Figure 5, we plot the averages of the absolute strengths of each component of the extrapolated fields at different heights, where the averages are calculated over each horizontal plane at the corresponding height. It can be found that the strength of the optimization field approaches evidently that of the potential field as the height increases. Note that as a whole, the profiles of these extrapolated field strengths are similar and the extrapolated field strengths are inclined to be the same values as the height increases. It can be seen that  $B_x$ s and  $B_y$ s of DBIE field are smaller than those of the potential field when the height is low, but they exceed those of the potential field as the height increases. For  $B_z$ s, the profiles of these field strengths are similar specially. It is noticed that the magnetic field strength decreases quickly/slowly as the height is below/above  $\sim 1000$  km. This trend is consistent for all the extrapolated fields. To further compare the strength differences of the NLFF fields ( $B_{NLFF}$ ) and the potential field ( $B_P$ ) quantitatively, the averages of  $|B_{NLFF} - B_P|$  for the three NLFF extrapolated fields at the corresponding height are given in Table 2, where  $B_{NLFF}$  and  $B_P$  are the total field strength of a given position in different horizontal planes. It can also be seen from Table 2, the amplitudes of the NLFF fields approach to that of the potential field as the height increases. The differences of the magnetic field strength between the NLFF fields and the potential field are of the order of 5 G on the photosphere, and this order drops to 0.1 G when the height reaches to  $\sim 2000$  km. The differences between the optimization field and the potential field approach zero as the height is above  $\sim 4000$  km.

In order to study the azimuth differences between the NLFF fields and the potential field, the probability density functions (PDF) of the shear angles at layers of  $z = 0, 545, 1090 \dots 4905$  km are plotted. In this paper, the shear angles is defined as the average over horizontal planes of the absolute value of the azimuth difference between the NLFF and the potential fields at different height. Figures 6, 7 and 8 show the PDFs of the shear angles of the optimization, DBIE and AVI fields, respectively. In Figure 6, for the optimization field, the shear angles decrease evidently with height, and the mean value (the average of the absolute values over each horizontal plane) changes from  $58^\circ$  at  $z = 0$  km to  $0^\circ$  as  $z > 4000$  km. For the DBIE field in Figure 7, the PDF profiles do not change evidently as the height increases. The mean values of the shear angles increase with the height up to  $z \sim 2725$  km, and decrease again above. In Figure 8, the mean



values of the shear angles of the AVI field increase slowly with height, and the mean value of the shear angles reaches  $72.2^\circ$  at  $z = 4905$  km. While the PDF profiles do not change significantly as  $z > 2180$  km.

In Figure 9, the distributions of the shear angles shown by the contour lines are overlaid on the grey-scale map of the LOS magnetic fields at three low layers of  $z = 0, 109, 545$  and  $1090$  km. The red contours are  $60^\circ, 80^\circ$  and  $100^\circ$ , and the blue ones  $-60^\circ, -80^\circ$  and  $-100^\circ$ . Although the mean values (the average of the absolute values) of the shear angles are different for those extrapolated fields, the distributions of the shear angles are very similar at the low layers, especially for DBIE and AVI methods. It can be found that the larger shear angles often appear near the edge of the strong vertical magnetic field. It also can be found that the magnetic field in the quiet Sun is inclined to be non-potential since there are evident shear angles on the photosphere ( $z = 0$  km).

#### 4. Discussions and Conclusions

Although theories and models have been proposed to describe the chromospheric and coronal magnetic field in the quiet Sun, it is still an open problem to know the true chromospheric and coronal magnetic fields. The magnetic field extrapolation is an alternative method to study the chromospheric and coronal magnetic fields, however there are limitations for applying the force-free extrapolation to the quiet Sun.

The application of magnetic field extrapolation to measured vector magnetograms of the active regions has been done with some success recently, which are based on two considerations: First, the reconstructed magnetic field can be assumed to be essentially force-free; Second, sunspots with extremely high flux concentrations are present in the vector magnetograms, so that the large-scale, coronal magnetic structures linked to them might be possibly determined by the dominant, largely force-free magnetic field only. On the other hand, for the quiet Sun the usage of the magnetic field extrapolation is less justified: the force-free assumption is not satisfied completely (the plasma  $\beta$  may be not low enough in the quiet Sun) and the magnetic flux in the quiet regions is concentrated on scales of the order of (or even smaller than) the spatial resolution in the normal magnetogram observations.

However, Kilogauss magnetic field has been found in the quiet Sun recently (*e.g.*, Stenflo 1973 and Wijn *et al.* 2009). Thus, the plasma may locally satisfy the condition of  $\beta < 1$  and the force-free assumption is met approximatively, which, however, is a problem worthy to investigate continually. Some authors have assumed the force-free requirement is satisfied in the quiet Sun and used LFF field extrapolation to study the properties of magnetic field in the quiet Sun (*e.g.*, Tu *et al.*, 2005; Régnier *et al.* 2008 and Zhao *et al.*, 2009). In our work, we also assume that the force-free requirement is satisfied in the quiet Sun and attempt to apply the NLFF magnetic field extrapolation to the quiet Sun. A quiet region with the high resolution observed by *Hinode* SOT/SP is chosen as the boundary to extrapolate the magnetic field up to  $\sim 5500$  km above the photosphere. Four magnetic field extrapolation methods are used to study the

magnetic fields in the quiet Sun, and the differences among these extrapolated fields are studied in detail.

In order to characterize the differences between the NLFF fields and the potential field in the quiet Sun, we analyze the magnetic field strengths and the transverse azimuths of the NLFF fields and the potential field. It is found that the field strength differences between the NLFF fields and the potential field decrease evidently as the height increases, although the amplitudes of these decrease are different among these three NLFF fields. It is found that when the height reaches to  $\sim 2000$  km, there are no evident differences between the NLFF fields and the potential field, since these differences are of the order of 0.1 G.

In the study of the transverse field azimuths, it is found that the photospheric magnetic field is non-potential because there are evident shear angles on the photosphere, the mean value of the shear angles is about  $58^\circ$  on the photosphere. As the height increases, the changes of shear angles are different among these three NLFF fields. The shear angle tends to decrease rapidly as the height increases for the optimization field, it increases gradually as the height increases for the AVI field, and it stays practically constant for the DBIE field. It is found that the larger shear angles often appear near the edge of the strong vertical magnetic fields, which are found to be very similar for three NLFF fields.

**Acknowledgements** We thank the anonymous referee for helpful comments and suggestions. *Hinode* is a Japanese mission developed and launched by ISAS/JAXA, collaborating with NAOJ as a domestic partner, NASA and STFC (UK) as international partners. Scientific operation of the *Hinode* mission is conducted by the *Hinode* science team organized at ISAS/JAXA. This team mainly consists of scientists from institutes in the partner countries. Support for the post-launch operation is provided by JAXA and NAOJ (Japan), STFC (U.K.), NASA, ESA, and NSC (Norway). This work was partly supported by the National Natural Science Foundation of China (Grant Nos. 10611120338, 10673016, 10733020, 10778723, 11003025 and 10878016), Important Directional Projects of Chinese Academy of Sciences (Grant No. KLCX2-YW-T04) and National Basic Research Program of China (Grant No. 2006CB806301).

## References

- Alissandrakis, C.E.: 1981, *Astron. Astrophys.* **100**, 197.  
 Almeida, J.S.: 1997, *Astron. Astrophys.* **324**, 763.  
 Aly, J.J.: 1989, *Solar Phys.* **120**, 19.  
 Amari, T., Aly, J.J., Luciani, J.F., Boulmezaoud, T.Z., Mikic, Z.: 1997, *Solar Phys.* **174**, 129.  
 Amari, T., Boulmezaoud, T.Z., Aly, J.J.: 2006, *Astron. Astrophys.* **446**, 691.  
 Chiu, Y. T., Hilton, H. H.: 1977, *Astrophys. J.* **212**, 837.  
 Chodura, R., Schlueter, A.: 1981, *J. Comput. Phys.* **41**, 68.  
 Cuperman, S., Bruma, C., Heristchi, D.: 1997, *Astron. Astrophys. Suppl.* **122**, 381.  
 DeRosa, M., Schrijver, C. J., Barnes, G., Leka, K. D., Lites, B. W., Aschwanden, M. J., Amari, T., Canou, A., McTiernan, J. M., Régnier, S., Thalmann, J. K., Valori, G., Wheatland, M. S., Wiegmann, T., Cheung, C. M., Conlon, P. A., Fuhrmann, M., Inhester, B., Tadesse, T.: 2009, *Astrophys. J.* **696**, 1780.  
 Demoulin, P.; Bagala, L. G.; Mandrini, C. H.; Henoux, J. C.; Rovira, M. G.: 1997, *Astron. Astrophys.* **325**, 305.  
 Dimitropoulou, M., Georgoulis, M., Isliker, H., Vlahos, L., Anastasiadis, A., Srintzi, D., Moussas, X.: 2009, *Astron. Astrophys.* **505**, 1245.  
 Dowdy, J. F., Jr., Rabin, D., Moore, R. L.: 1986, *Solar Phys.* **105**, 35.

- Gabriel, A. H.: 1976, *Phil. Trans. R. Soc. London* **A281**, 339.
- Gary, G.A.: 1989, *Astron. Astrophys. Suppl.* **69**, 323.
- Giovanelli, R.G.: 1980, *Solar Phys.* **68**, 49.
- Harvey, J. W.: 2006a, *ASP Conference Series*, **358**, 419.
- Harvey, J. W.: 2006b, 26th IAU Joint Discussion, **3**, p.16-17.
- He, H., Wang, H.: 2008, *J. Geophys. Res.* **113**, A05S90.
- He, H., Wang, H., Yan, Y.H.: 2008, 37th COSPAR Scientific Assembly, p.1197.
- Ichimoto, K., Lites, B., Elmore, D., Suematsu, Y., Tsuneta, S., Katsukawa, Y., Shimizu, T., Shine, R., Tarbell, T., Title, A.: 2008, *Solar Phys.* **249**, 233.
- Jing, J., Wiegelmann, T., Suematsu, Y., Kubo, M., Wang, H.: 2008, *Astrophys. J.* **676**, L81.
- Kosugi, T., Matsuzaki, K., Sakao, T., Shimizu, T., Sone, Y., Tachikawa, S., Hashimoto, T., Minesugi, K., Ohnishi, A., Yamada, T.: 2007, *Solar Phys.* **243**, 3.
- Lites, B. W., Rutten, R. J., Berger, T. E.: 1999, *Astrophys. J.* **517**, 1013.
- Metcalf, T. R., Leka, K. D., Barnes, G., Lites, B. W., Georgoulis, M. K., Pevtsov, A. A., Balasubramaniam, K. S., Gary, G. A., Jing, J., Li, J.: 2006, *Solar Phys.* **237**, 267.
- Metcalf, T.R., Jiao, L., McClymont, A. N., Canfield, R.C., Uitenbroek, H.: 1995, *Astrophys. J.* **439**, 474.
- Moon, Y.J., Choe, G. S., Yun, H. S., Park, Y. D., Mickey, D. L.: 2002, *Astrophys. J.* **568**, 422.
- Philip, J.: 2008, *Astrophys. J.* **683**, L87.
- Régnier, S., Amari, T.: 2004, *Astron. Astrophys.* **425**, 345.
- Régnier, S., Amari, T., Kersalé.: 2002, *Astron. Astrophys.* **392**, 1119.
- Régnier, S., Priest, E. R.: 2007, *Astron. Astrophys.* **468**, 701.
- Régnier, S., Parnell, C.E., Haynes, A.L.: 2008, *Astron. Astrophys.* **484**, L47.
- Sakurai, T.: 1981, *Solar Phys.* **69**, 343
- Schrijver, C. J., DeRosa, M. L., Metcalf, T., Barnes, G., Lites, B., Tarbell, T., McTiernan, J., Valori, G., Wiegelmann, T., Wheatland, M. S., Amari, T., Aulanier, G., Dmèoulin, P., Fuhrmann, M., Kusano, K., Régnier, S., Thalmann, J. K. 2008, *Astrophys. J.* **675**, 1637.
- Schrijver, C.J., DeRosa, M., Metcalf, T., Liu, Y., Mctierana, J., Régnier, S., Valori, G., Wheatland, M.S., Wiegelmann, T.: 2006, *Solar Phys.* **235**, 161.
- Schrijver, C.J., Title, A.M.: 2003, *Astrophys. J.* **597**, L165.
- Seehafer, N.: 1978, *Solar Phys.* **58**, 215.
- Song, M.T., Fang, C., Tang, Y.H., Wu, S.T., Zhang, Y.A.: 2006, *Astrophys. J.* **649**, 1084.
- Song, M.T., Fang, C., Zhang, H.Q., Tang, Y.H., Wu, S.T., Zhang, Y.A.: 2007, *Astrophys. J.* **666**, 491.
- Tsuneta, S., Ichimoto, K., Katsukawa, Y., Nagata, S., Otsubo, M., Shimizu, T.: 2008, *Solar Phys.* **249**, 167.
- Tu, C.Y., Zhou, C., Marsch, E., Xia, L.D., Zhao, L., Wang, J.X., Wilhelm, K.: 2005, *Sice.* **308**, 519.
- Stenflo, J.O.: 1973, *Solar Phys.* **32**, 41
- Valori, G., Kliem, B., Fuhrmann, M.: 2007, *Solar Phys.* **245**, 263
- Wang, H.: 1997, *Solar Phys.* **174**, 265.
- Wang, H., Yan, Y., and Sakurai, T.: 2001, *Solar Phys.* **201**, 323.
- Wang, T., Zhang, H. and Xu, A.: 1994, *Solar Phys.* **155**, 99.
- Wheatland, M.S., Sturrock, P.A., Roumeliotis, G.: 2000, *Astrophys. J.* **540**, 1150.
- Wiegelmann, T.: 2004, *Solar Phys.* **219**, 87.
- Wiegelmann, T., Inhester, B., Sakurai, T.: 2006, *Solar Phys.* **233**, 215
- Wijn, A.G.de, Stenflo, J.O., Solanki, S.K., Tsuneta, S.: 2009, *Space Sci. Rev.* **144**, 275
- Woodard, M. F., Chae, J. C.: 1999, *Solar Phys.* **184**, 239.
- Wu, S.T., Sun, M.T., Chang, H.M., Hagyard, M.J., Gary, G.A.: 1990, *Astrophys. J.* **362**, 698.
- Yan, Y., Li, Z.: 2006, *Astrophys. J.* **638**, 1162
- Yan, Y., Sakurai, T.: 2000, *Solar Phys.* **195**, 89.
- Zhang, H.Q.: 1996, *Astron. Astrophys. Suppl.* **119**, 205.
- Zhang, H.Q and Zhang, M.: 2000a, *Solar Phys.* **196**, 269.
- Zhang, M., Zhang, H.Q., Ai, G.X., Wang, H.N.: 1999, *Solar Phys.* **190**, 79.
- Zhang, M., Zhang, H.Q.: 2000b, *Solar Phys.* **194**, 29.
- Zhao, M., Wang, J.X., Jing, C.L., Zhou, G.P.: 2009, *Chin. J. Astron. Astrophys.* **9**, 933.

**Table 1.** The values of  $\sigma_J$ ,  $\langle |f_i| \rangle$ ,  $F_{max}$  and  $\epsilon$  for the potential and three NLFF extrapolated fields.

Method	$\sigma_J$ (Rad)	$\langle  f_i  \rangle$ $1 \times 10^{-4}$	$F_{max}$ $(G^2 M^{-1}) \times 10^{-11}$	$\epsilon$
Pote.	0.50	0.06	0.55	1.00
Opti.	0.97	0.23	1.21	1.98
DBIE	0.92	1.01	0.92	2.01
AVI	0.89	2.93	0.45	2.81

**Table 2.** The average of  $|B_{NLFF} - B_P|$  for three NLFF extrapolated fields at different heights.

Method	$ B_{NLFF} - B_P $ (G)				
	Height (km)				
	$z = 0$	$z = 1090$	$z = 2180$	$z = 3270$	$z = 4360$
Opti.	4.6713	0.0591	0.0091	0.0007	0.0001
DBIE	4.6713	0.5490	0.0748	0.1544	0.1628
AVI	4.6713	0.5226	0.1068	0.0895	0.1162

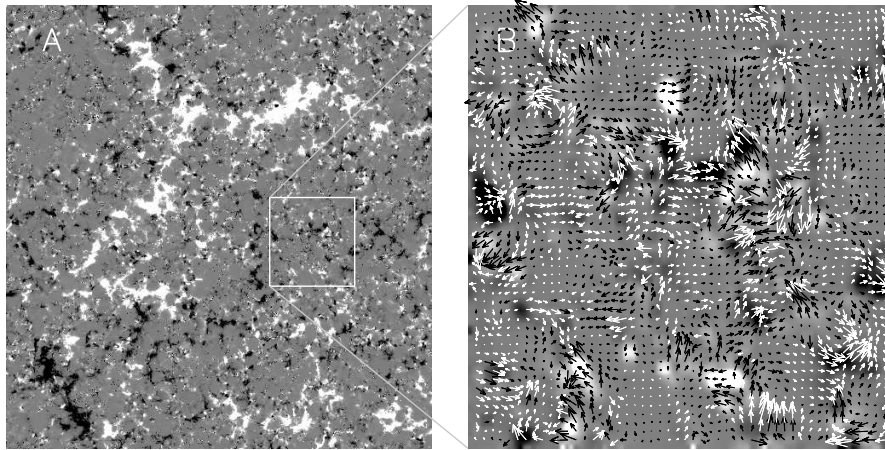


**Figure 1.** Left (A): line-of-sight (LOS) magnetic field observed from 00:23 UT to 01:48 UT on April 16, 2007. Right (B): the vector magnetogram of the region marked in the left panel with the white rectangle. The background image is the LOS magnetic field and the arrows stand for the transverse magnetic field.

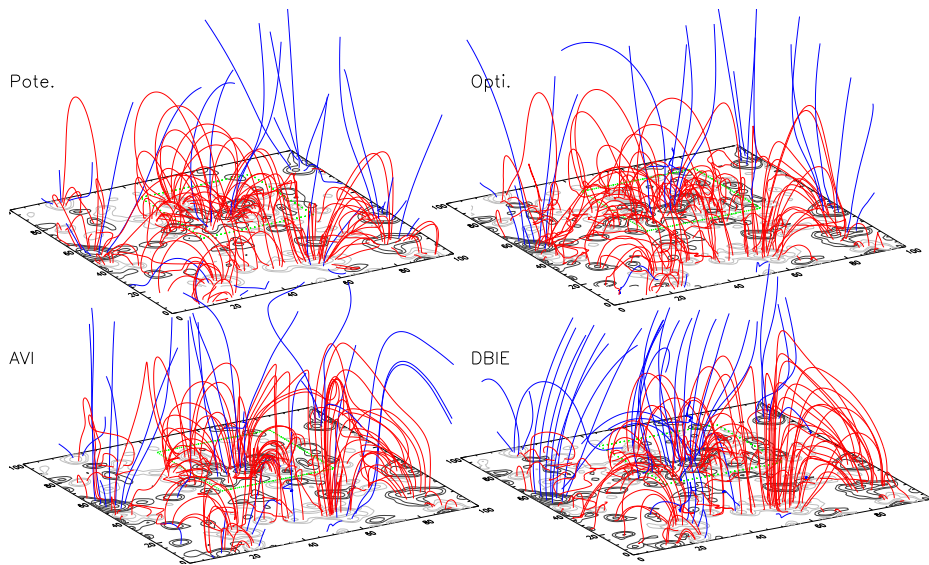


**Figure 2.** The magnetic field lines for three NLFF fields (Opti, AVI and DBIE) and a potential field.

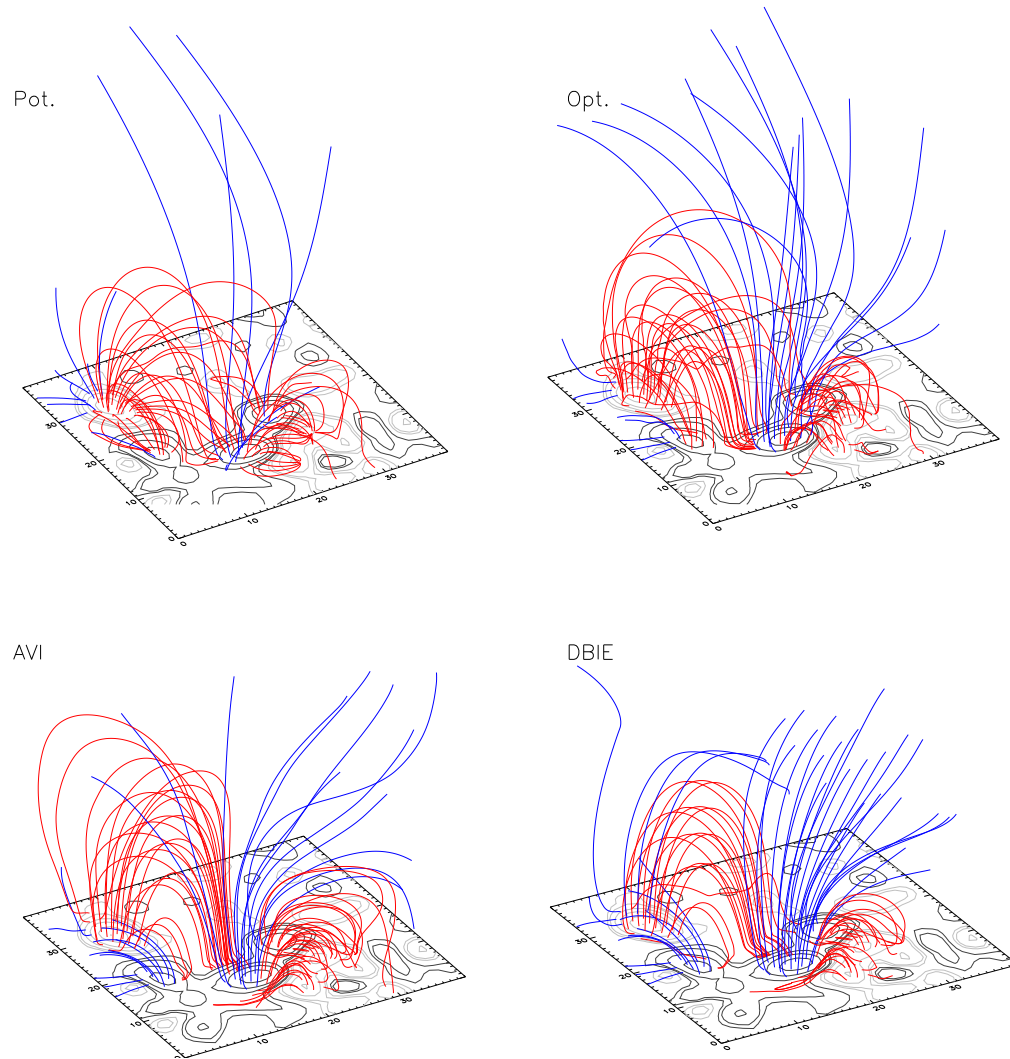


**Figure 3.** The magnetic field lines for three NLFF fields (Opti, AVI and DBIE) and a potential field, starting within the sub-region labeled by a green square in Fig 2.

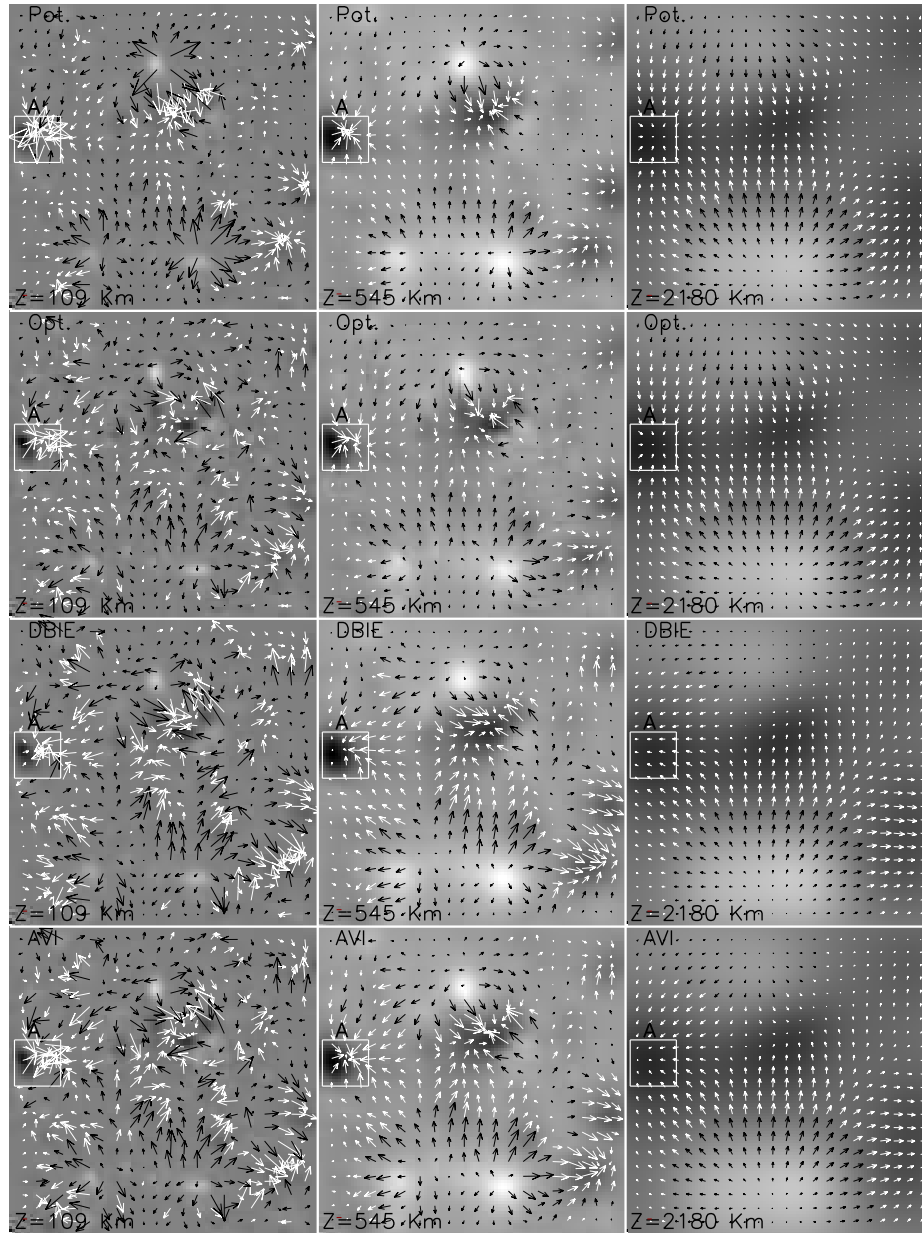


**Figure 4.** Vector magnetograms of extrapolated field at the heights of  $z = 109, 545$  and  $2180$  km. The background image is the LOS magnetic field and the black and white arrows stand for transverse magnetic field. The rows 1, 2, 3 and 4 correspond to the potential field, three NLFF fields extrapolated with optimization, DBIE and AVI method, respectively. The columns 1, 2 and 3 show different heights.

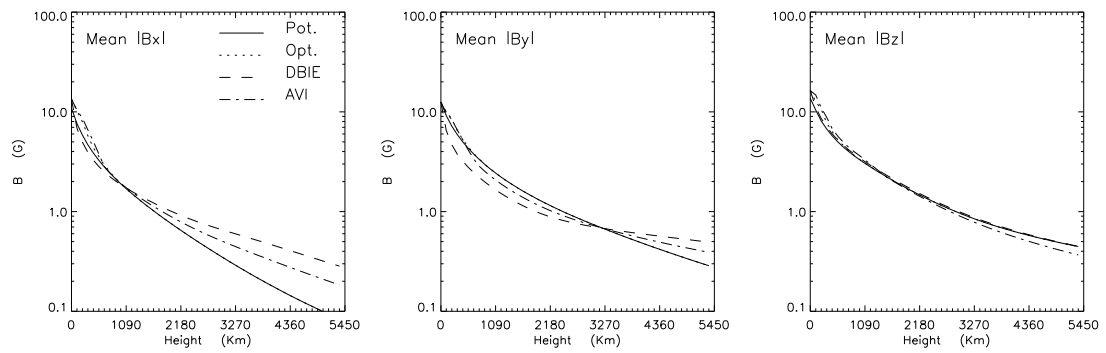


**Figure 5.** The average of absolute strengths of  $B_x$ ,  $B_y$  and  $B_z$  of the extrapolated magnetic field versus the height, the different style lines indicate the extrapolation methods used.



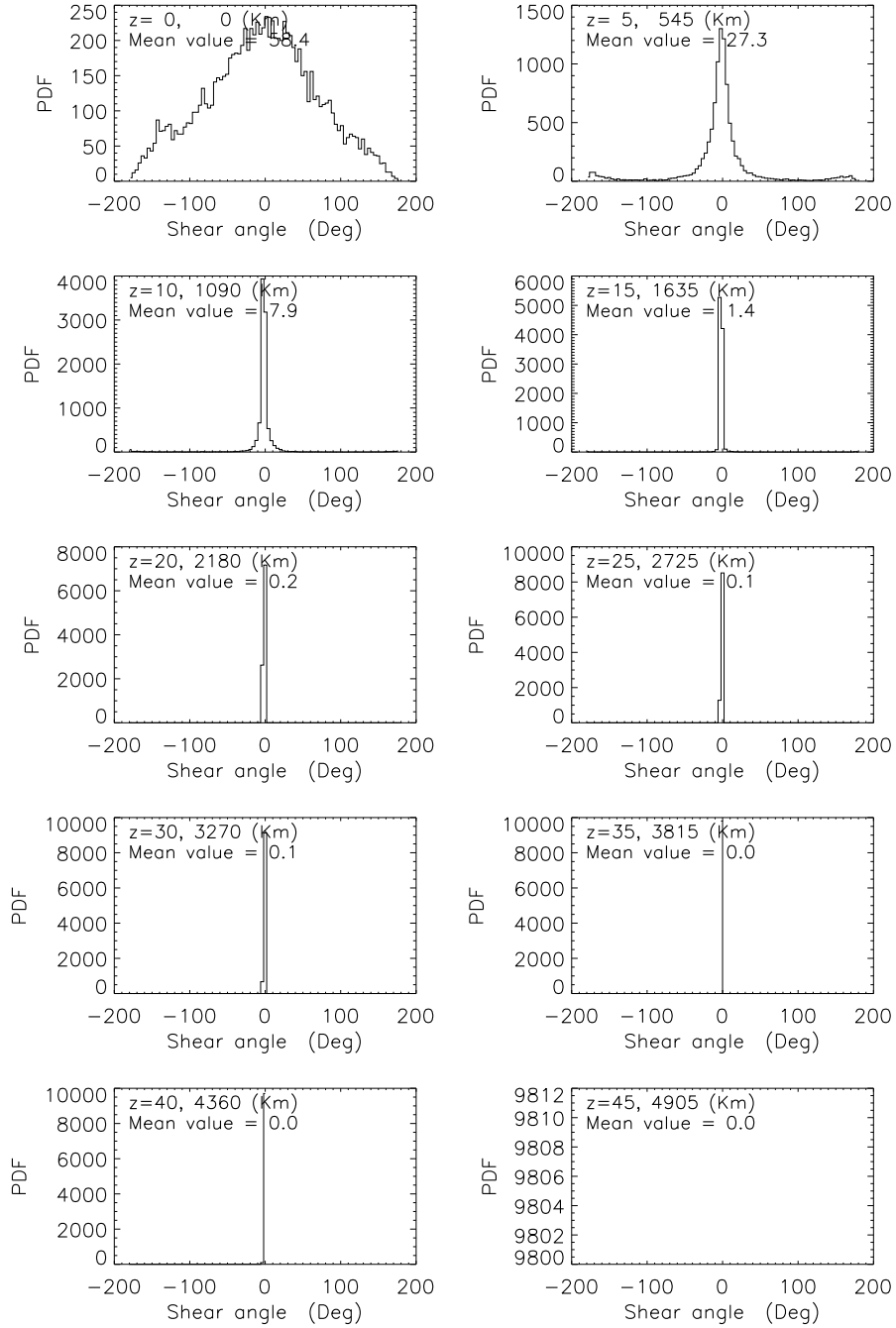


**Figure 6.** The PDF of the shear angles at different layer ( $z = 0, 545, 1090 \dots 4905$  km) for optimization method. Mean value plotted in each panel is the average of the absolute value of the shear angle.

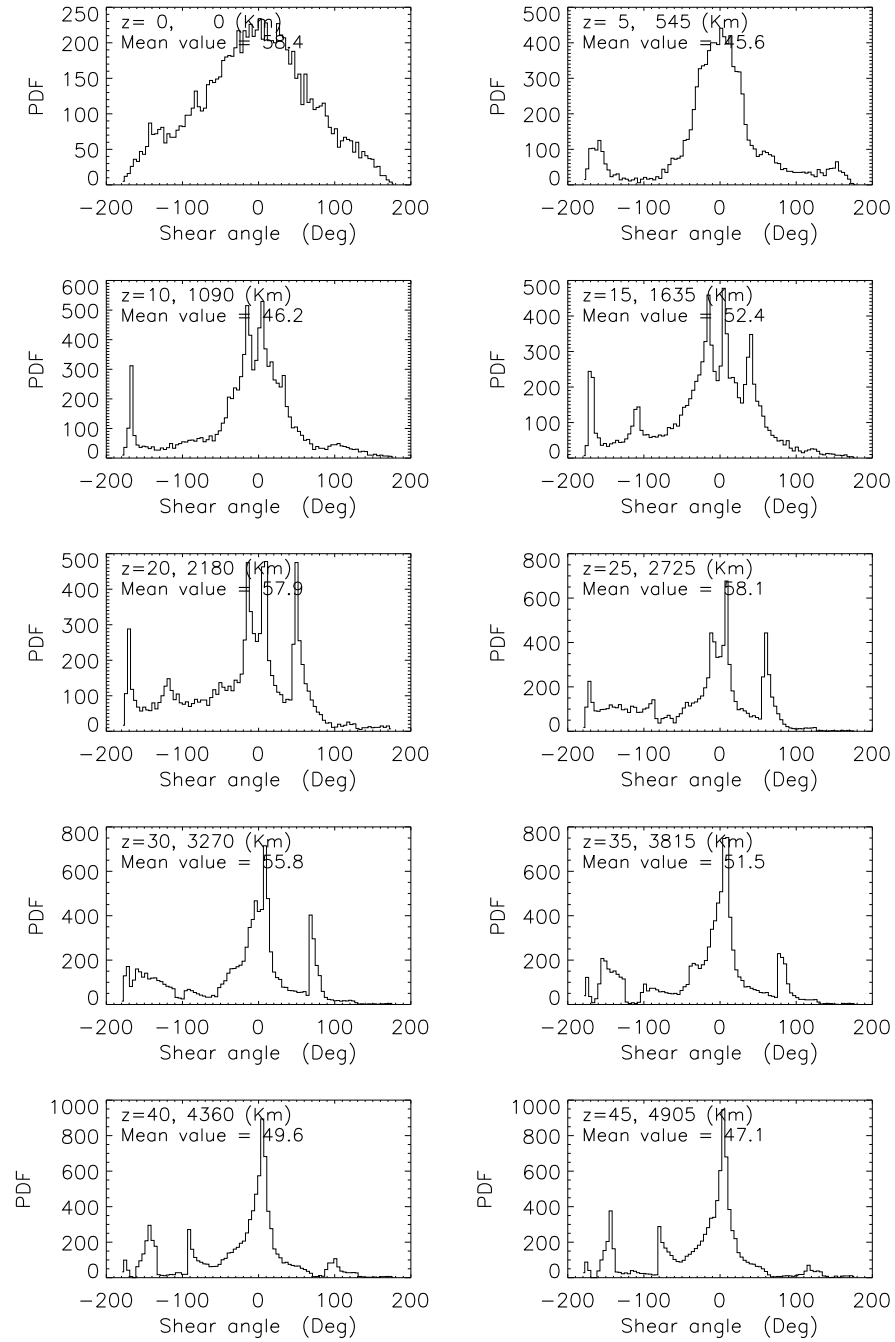


Figure 7. Same as Figure 6 but for DBIE method.

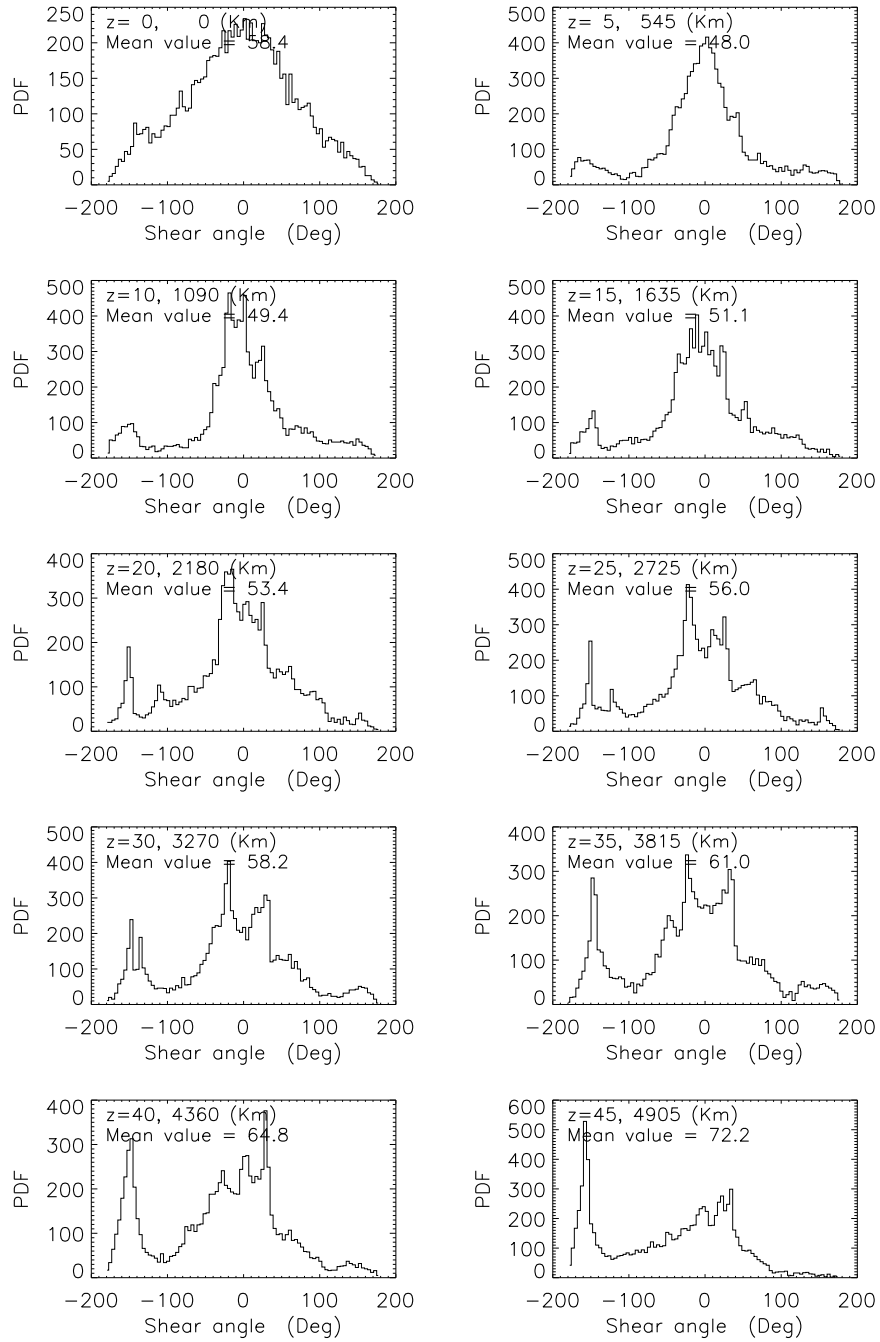
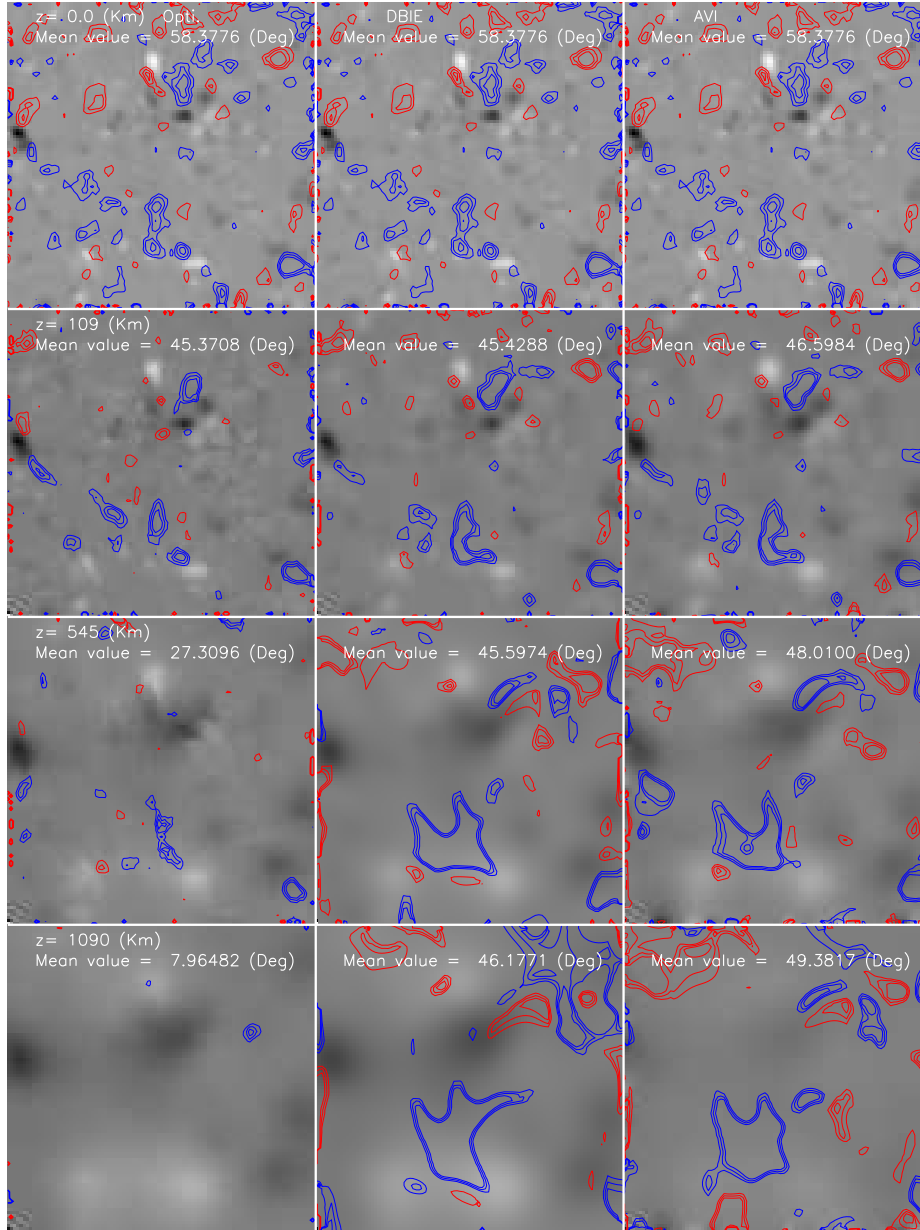


Figure 8. Same as Figure 6 but for AVI method.



**Figure 9.** The distributions of the shear angles at different layer ( $z = 0, 109, 545$  and  $1090$  km) for three NLFF extrapolated fields. The contours are  $\pm 60^\circ, 80^\circ, 100^\circ$  and red/blue contours represent positive/negative values. The columns 1, 2 and 3 correspond to the optimization, DBIE and AVI method, and the rows 1, 2, 3, and 4 are for  $z = 0, 109, 218$  and  $327$  km, respectively. The mean value reported in each panel is the average of the absolute value of the shear angle.